

The Shoemaker-Levy 9 H impact: some results from the William Herschel Telescope

J.L. Ortiz^{1,2}, G. Orton¹, F. Moreno², A. Molina^{2,3}, S. Larson⁴, and P. Yanamandra-Fisher¹

¹ Jet Propulsion Laboratory, California Institute of Technology, 4800 Oak Grove Drive, Pasadena, CA 91109, USA

² Instituto de Astrofísica de Andalucía, CSIC, Aptdo 3004, E-18080 Granada, Spain

³ Departamento de Física Aplicada, Univ. Granada, Spain

⁴ Lunar and Planetary Laboratory, Univ. Arizona, Tucson, USA

Received 3 September 1996 / Accepted 6 December 1996

Abstract. We present a CCD lightcurve for the H impact observed at 948 nm by the 4.2-m William Herschel Telescope at La Palma (Spain). We compare the results with other lightcurves at visible and near infrared. There appears to be a common pattern in all the CCD lightcurves: An initial relative maximum is followed by a relative minimum and another maximum. Considering the plume as a superposition of material ejected at various speeds, we suggest the first maximum is likely due to reflected solar light by the plume at its widest phase. The minimum may be due to the disappearance of part of the plume, as the material ejected with vertical velocities lower than 9 km/s descends in its ballistic trajectory and penetrates below the level of solar illumination. The following maximum is most likely due to thermal emission from the reimpacting ejecta (either from the particulates or the gas). The timing of the second maximum and the moment of detection of the plume suggest vertical velocities in the range 9–12 km/s for most of the ejecta, with peak particle concentration at 11 km/s for the L impact, according to our interpretation of Schleicher et al. (1994) lightcurve. The atmospheric level where the visible emission takes place is estimated to be $P = 25^{+65}_{-25}$ mbar and $P = 35^{+30}_{-35}$ mbar for the L and H impacts, respectively.

Key words: comets: Shoemaker-Levy 9 – Jupiter

1. Introduction

So far, near-infrared lightcurves (mainly at 2.3 μm) have been presented by many groups (see e.g., Herbst et al., 1995, Hamilton et al., 1995, Orton et al., 1995, Graham et al., 1995, Nicholson et al., 1995, Takeuchi et al., 1995) and a clear picture has emerged in which at least three different kinds of phenomena are identified by the three different features common to all near infrared lightcurves: first precursor, second precursor and main

peak. The associated phenomena are bolide, fireball and fall-back phase, respectively. In addition, after the main peak, some lightcurves show a “shoulder” whose origin is still unclear, but may be due to re-entering material “bouncing” of the top of the atmosphere and re-entering a second time (Nicholson, 1996).

However, lightcurves at wavelengths below 1 μm have not been compared with them, to present at least a phenomenology consistent with all of the major impacts, as it is the case for the 2.3- μm lightcurves. Unfortunately, Hubble Space Telescope (HST) did not observe the time evolution of any of the plumes using the same filter for all the exposures (alternating between filters instead, in order to maximize the probability of plume detection (Hammel et al., 1995)). Hence, HST cannot provide the data set needed to study the evolution of the flux.

Only a few impacts generated large enough plumes to be detected clearly in the visible by observing sites with good seeing. Hence, the data sets showing impact phenomena are very scarce. From those few known to us, there is a minimum between two maxima in the H lightcurve (which we present here) from the 4.2-m WHT telescope (La Palma, Spain) at 948 nm. An analog minimum between two maxima was observed for L impact by Schleicher et al. (1994) at 892 nm, and by Fitzsimmons et al. (1996) at 907 nm. Hence, there seems to be a common pattern in all “visible” lightcurves.

In this paper, we present the WHT data on H in the section labeled “Observational results”. These observations were made as part of the Comet Impact Network Experiment (CINE). In the section “Definitions and geometric analysis”, we offer an explanation for the phenomenology seen in all lightcurves based on geometrical computations and timing arguments for a ballistic plume. In the section “Discussion and comparison with near infrared lightcurves”, we discuss the results obtained for H and use some data on L impact by Schleicher et al. (1994) and Fitzsimmons et al. (1996) to derive some physical properties. We also compare some predictions on near-infrared features from our analysis with measured near-infrared lightcurves.

Send offprint requests to: J.L. Ortiz, ortiz@iaa.es

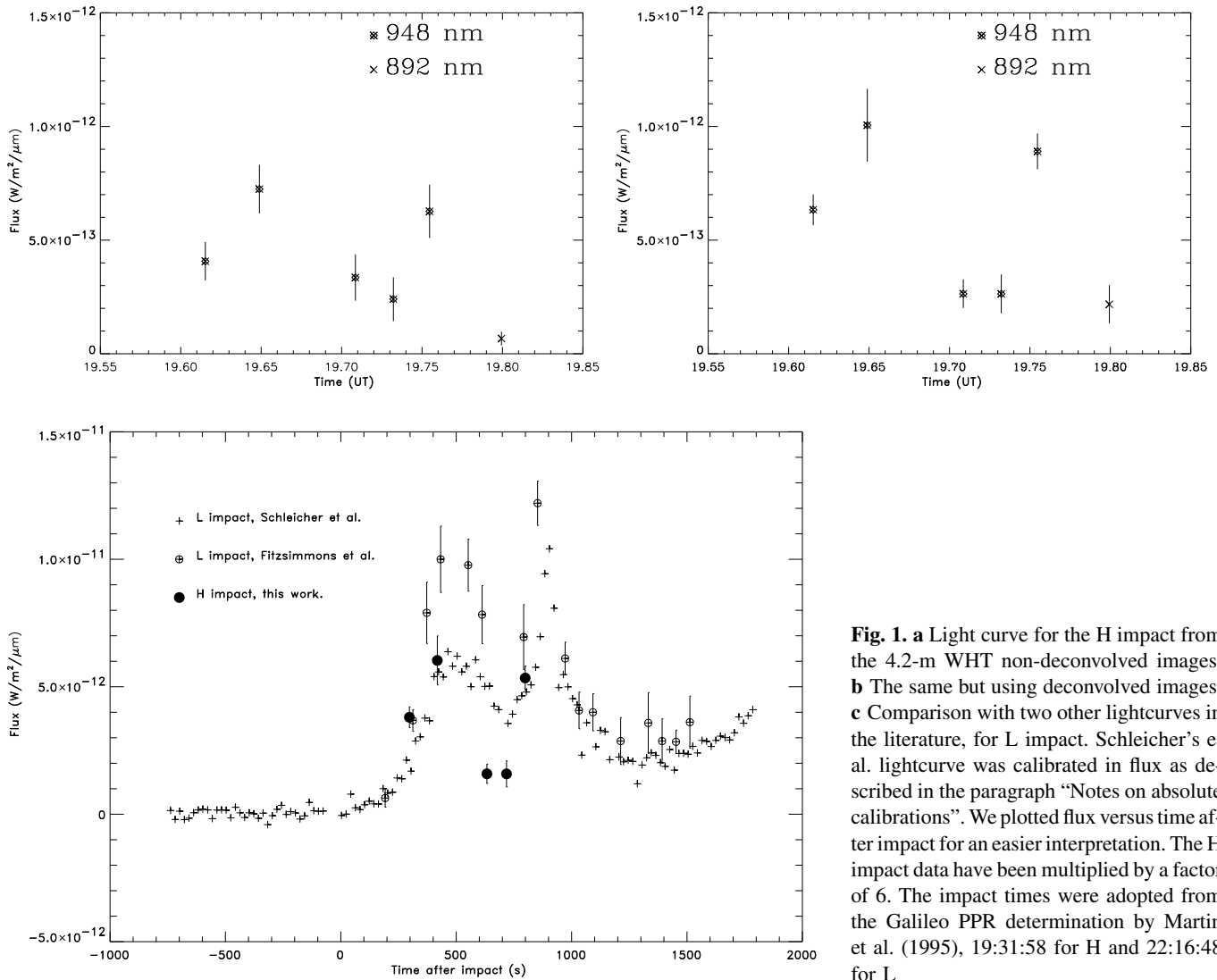


Fig. 1. **a** Light curve for the H impact from the 4.2-m WHT non-deconvolved images. **b** The same but using deconvolved images. **c** Comparison with two other lightcurves in the literature, for L impact. Schleicher’s et al. lightcurve was calibrated in flux as described in the paragraph “Notes on absolute calibrations”. We plotted flux versus time after impact for an easier interpretation. The H impact data have been multiplied by a factor of 6. The impact times were adopted from the Galileo PPR determination by Martin et al. (1995), 19:31:58 for H and 22:16:48 for L

2. Observational results

In Figs. 1a, 1b we present the H lightcurve (impact flux versus time) in absolute units at 948 nm as observed from the 4.2-m WHT. We also present a flux value at 892 nm after the second maximum. In Fig. 2, we present the sequence of images which show the plume development analyzed here. The detection of the H impact plume was already presented by Larson et al. (1994).

The first image of the sequence is the first image obtained by the telescope. No previous images were taken because it was twilight. The instrumental set up, used previously (Moreno et al., 1995) includes a 1280×1180 coated EEV P88300 CCD and interference filters centered at 948 nm and 892 nm with a full width at half maximum of 50 Å. Plots of their transmission curves can be found in Ortiz (1994). The plate scale was 0.102 ± 0.002 arcsec/pixel. Integration times are shown in the caption of Fig. 2.

To generate the lightcurve in Fig. 1a, we first removed the bias and flatfielded the images. After that we interpolated over bad pixels, fit an ellipse to the limb of the planet, centered,

and rotated the jovian images. We selected the location of the plume in each image by visual inspection. This location moved a few pixels mainly along the E-W direction because of both the rotation of Jupiter and the ballistic motion. We integrated the signal within a 0.51×0.51 arcsec square aperture, subtracted the sky contribution and subtracted Jupiter’s contribution. The result was divided by the sum of all the data numbers from Jupiter and calibrated in flux as described in the section “Notes on absolute calibrations”. The sky contribution was computed using the mean count rate from five aperture positions in the sky. The jovian contribution was determined by placing three apertures ~ 2 arcsec apart from the plume position, sampling only the limb of Jupiter (see Fig. 3).

Sky noise is the main source of uncertainty in our lightcurve. This is shown in Fig. 1 as the standard deviation of the 5 sky positions. Another source of uncertainty was the size of the aperture and the jovian contribution.

The size of the aperture was too small to include all the flux from the plume, which is spread by the seeing. However, a larger aperture size resulted in a considerable increase in uncertainty

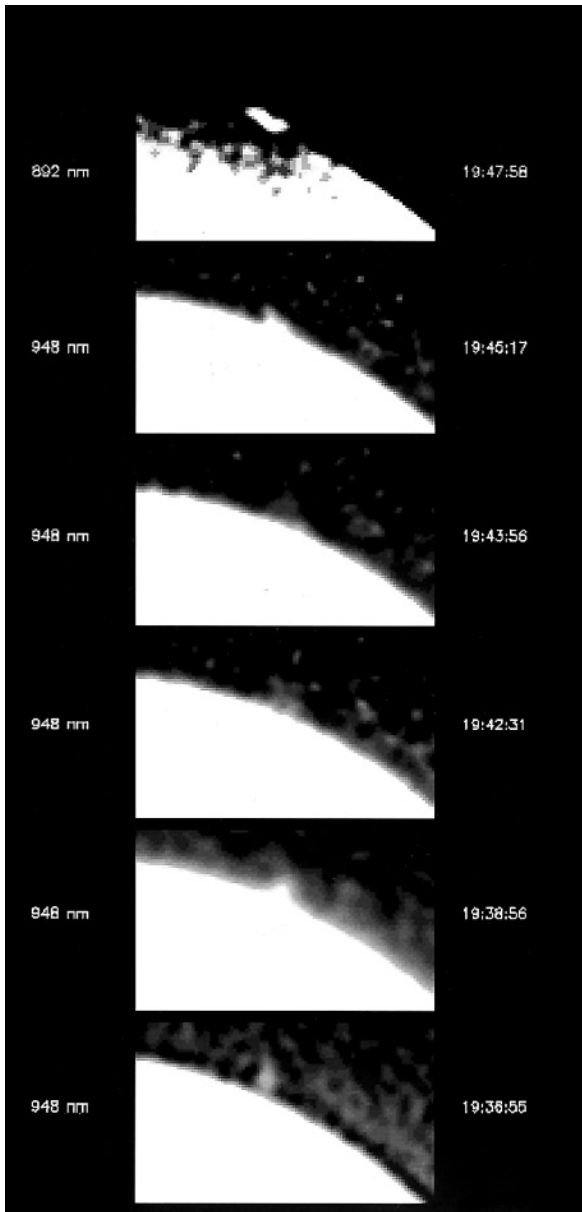


Fig. 2. Sequence of images which show the evolution of the H plume. The contrast has been enhanced so that the plume can be easily seen. Integration times were 4s, 4s, 2s, 2s, 2s and 2s

arising from the sky noise. As seeing remained very stable during the sequence, we estimated that a constant percentage of the flux (20 to 40%) was outside the aperture in all the images. The uncertainty in the removal of the jovian contribution was estimated to be $2 \cdot 10^{-13} \text{ W m}^{-2} \mu\text{m}^{-1}$, derived by computing the dispersion from 3 different apertures located 1 to 2 arcsec from the plume at slightly different positions (see Fig. 3). This uncertainty is more than an order of magnitude smaller at 892 nm. The uncertainty in time is assumed to be less than 1 s because the computer was linked to a GPS receiver. The gaps between observations are the result of the long times needed to read the CCD and the time needed to operate the computer. Between the

Table 1. H impact fluxes

UT Time	Flux ($\text{W m}^{-2} \mu\text{m}^{-1}$)	Error	λ (nm)
19:36:55	$6.2 \cdot 10^{-13}$	$0.6 \cdot 10^{-13}$	948
19:38:56	$1.0 \cdot 10^{-12}$	$1.6 \cdot 10^{-13}$	948
19:42:31	$2.7 \cdot 10^{-13}$	$0.6 \cdot 10^{-13}$	948
19:43:56	$2.7 \cdot 10^{-13}$	$0.8 \cdot 10^{-13}$	948
19:45:17	$8.9 \cdot 10^{-13}$	$0.8 \cdot 10^{-13}$	948
19:47:58	$2.2 \cdot 10^{-13}$	$0.8 \cdot 10^{-13}$	892

second and third images analyzed here, two frames were taken by reading only a small “subwindow” of the CCD in order to save time. Unfortunately, this mode did not work properly and the resulting images were not useable.

We obtained a better estimate of the flux by using deconvolved images. The improvement in spatial resolution allows for the use of small apertures. We deconvolved our images using a Lucy (1984) algorithm and a model for the point spread function which worked well for planetary images (Ortiz, 1994). The lightcurve using a 0.51×0.51 arcsec square aperture is shown in Fig. 1b. These fluxes are listed in Table 1.

Although the time resolution is not very good, the data show the typical pattern already discussed. In the lightcurve (Fig. 1a, 1b) there is a maximum followed by a minimum, and another maximum. The maximum flux at $2.3 \mu\text{m}$ was observed at $19:44:30 \pm 45\text{s}$ UT, (Hamilton et al., 1995), which is 19.74 UT, earlier than the second maximum at 948 nm. The shape of the WHT lightcurve corresponds closely with the maximum, minimum and second maximum in CCD lightcurves for L (Schleicher et al., 1994; Fitzsimmons et al., 1996), also plotted in Fig. 1c. Again, the second maximum in these CCD lightcurves (which occurred at 22:31:52 according to Schleicher et al., 1994) is observed after the main peak at IR wavelengths, which took place at about 22:30 UT (Lagage et al., 1995). The difference is close to 2 minutes. We note that there is an order of magnitude difference between the peak fluxes of the H and L impact CCD lightcurves.

3. Definitions and geometric analysis

Here, we use the term ejecta to denote the material ejected by the explosion after fragment entry. We assume this material is ejected in a variety of ballistic trajectories. We have generated synthetic trajectories for ballistic material, for different sets of parameters (initial velocity, altitude of explosion from the 100-mbar level, impact longitude from Midnight Meridian and terminator longitude from Midnight Meridian). The altitude of these trajectories is plotted versus time in Fig. 4, along with the minimum height that the impact ejecta should have reached to be observable in sunlight. The parameters used are those for H and L (Chodas and Yeomans, predictions as of July 16) with a zero altitude set to the 100-mbar level and assuming 45° trajectories. Hereafter in the text, we will cite only the vertical component of the velocity.

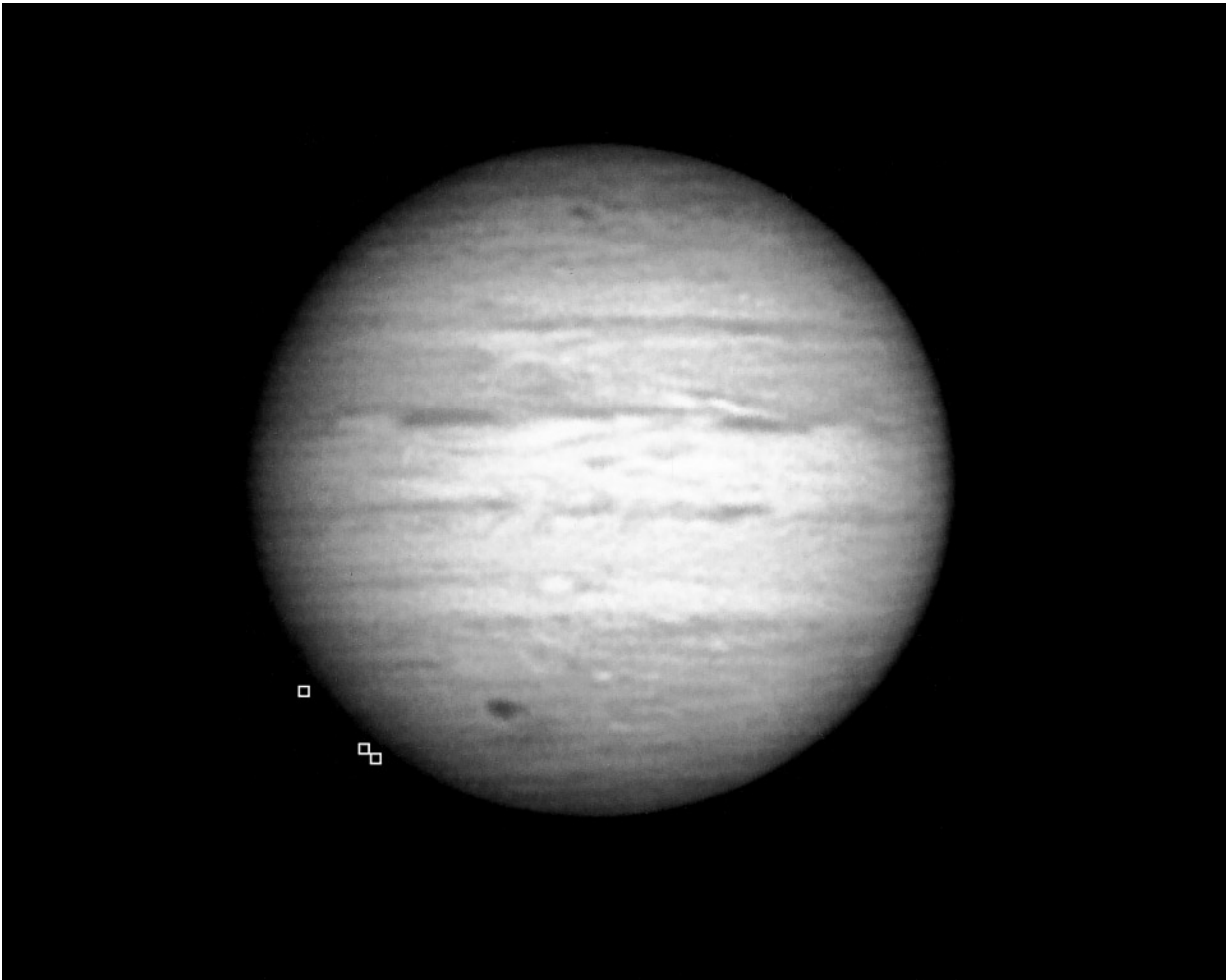


Fig. 3. Image representative of the set analyzed here. It is shown in linear stretch. The three boxes show the positions we used to measure Jupiter's contribution to the impact aperture. We do not have stellar images to accurately determine the point spread function, but some of the details observed in this image subtend less than 0.4 arcsecs

The terminator level was also assumed to be at 100 mbar. The jovian radius at -43° and 100 mbar was obtained by correcting for oblateness the 100-mbar equatorial radius. The gravity acceleration was corrected for oblateness in the following way: $23.22 + 2.85 \sin^2(\text{latitude})$ (where 23.22 m/s^2 is the equatorial gravity acceleration, in Jupiter, Anderson, 1976). The gravitational acceleration has also been corrected for altitude in each step. Coriolis correction has not been applied (this does not have an important effect on the vertical component). Refraction effects would have a minor influence on the very lower parts of the trajectories and have been ignored (see Hammel et al., 1995). Note that the horizontal velocity of the plumes plays an important role in lowering the level where the plumes reach sunlight (see Figs. 4a, 4b).

The moment of first detection of the plumes provides information on the maximum plume vertical velocity or, at least, on the fastest ejecta which carry a sufficient amount of material to be visible in sunlight. From the work by Schleicher et al. (1994), the first indication of the plume is 220 ± 20 seconds after the L impact, the beginning of the flux increase in their lightcurve.

Fitzsimmons et al. (1996) report their first detection about 210 s after impact. The 220 ± 20 -sec time is consistent with plume velocity of $9 \pm 1 \text{ km/s}$, as can be seen in Fig. 4a (intersection of vertical trajectory with the curve of sun illumination level for its corresponding velocity). This is best seen in Fig. 5, which shows an enlarged version of Fig. 4a along with the curve for 3.5-km/s ejecta. The first detection of H from the WHT data is somewhat later (300 s) which would suggest slightly slower ejecta. On the other hand, the telescope was not observing earlier, so this value represents a lower limit. For L, we believe most of the material is ejected at velocities between 9 and 12 km/s, since, for that velocity range, the material returns to the original level between 780 and 1000 seconds after impact, which is the time of rise and decline of the second maximum in the lightcurve of Schleicher et al. We believe this maximum is due to thermal emission. The maximum itself occurs when the 11 km/s-material returns to the original altitude (~ 900 sec after impact). Then, for the L impact, we conclude that the largest amount of material optically thick in the visible is ejected at 11 km/s, but there is also material thrown at other velocities, with a maximum of 12 km/s. We

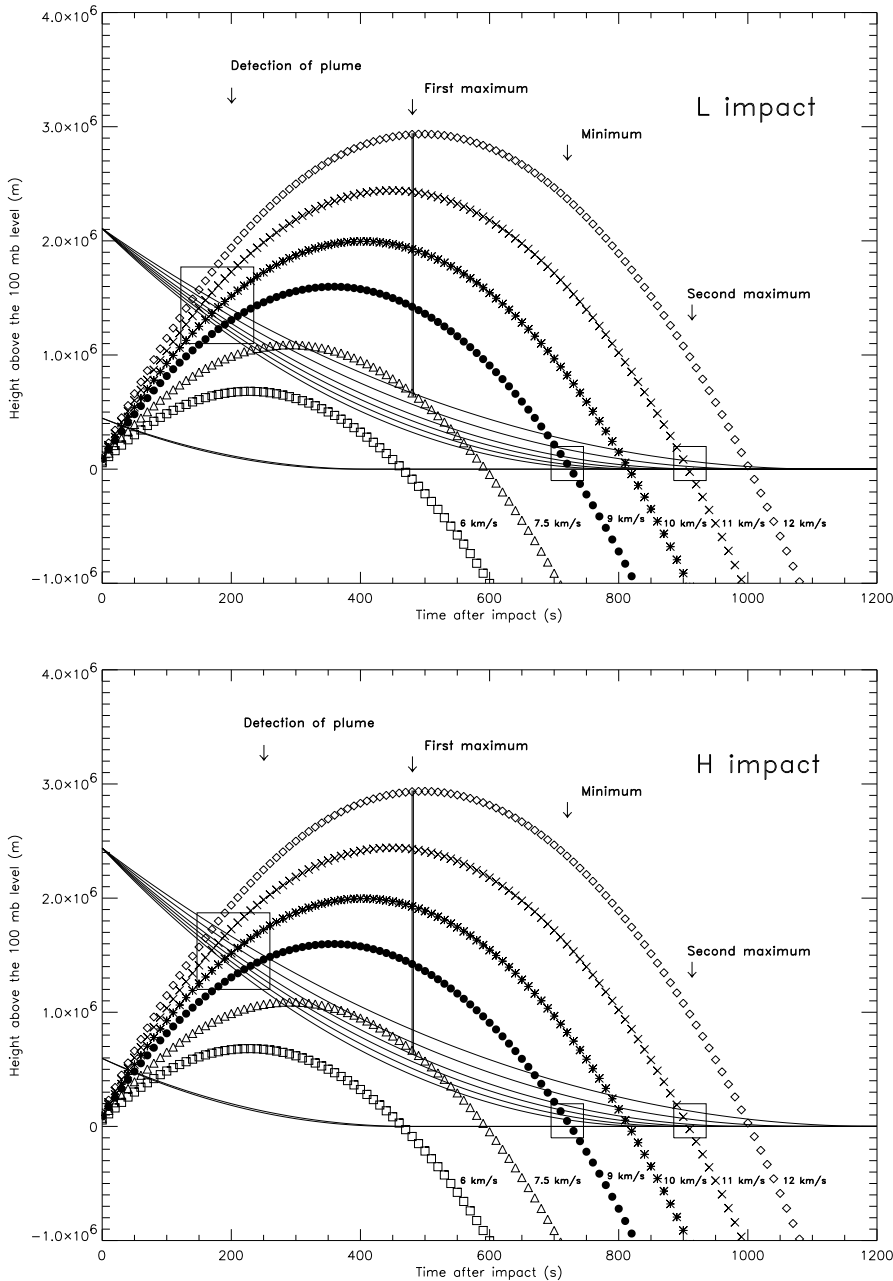


Fig. 4. **a** Height above the 100-mbar level as a function of time after impact L for ejecta with several vertical velocities, as indicated in the labels. The continuous lines represent the minimum height above which the ejecta are visible in sunlight. The upper continuous line corresponds to 6 km/s and the lower corresponds to 12 km/s. As can be seen, the 6-km/s ejecta do not intercept the curve of the sunlit height corresponding to 6 km/s. That means that the 6-Km/s ejecta cannot be visible in reflected sunlight. Also plotted in continuous lines at the bottom of the graph is the minimum height that the ejecta should have to be visible in emission, as a function of time, for the 12-km/s and 6-km/s ejecta. **b** The same as **a** but for H impact. The boxes in **a** and **b** represent particularly interesting regions discussed in the text

can make comparisons with the G impact results, as both G and L are in the same class in the categorization scheme of Hammel et al., releasing similar amounts of energy and leaving similar scars, etc. This maximum velocity of 12 km/s is in agreement with the velocity derived by Hammel et al. (1995) for the highest velocity ejecta in G plume by measuring its highest altitude, a completely different approach to that followed here, which is based on timings. For the H impact, the time of the second maximum from Fig. 1 is much more uncertain, but seems to be shorter than what we would expect for 11 km/s ejecta. This would require slower ejecta, which would be consistent with the observations of a smaller energy release in H impact compared to L and a smaller crescent-shaped scar.

The first maximum is reached when most of the ejected material is above the sunlit limit and with its maximum vertical spreading. For L, taking a section in Fig. 4a we observe that the maximum spreading (while all the 7.5–12 km/s material is still in sunlight) corresponds to time $\simeq 500$ s. This value is in perfect agreement with the time of maximum shown in the lightcurve of Schleicher et al. (1994) and with the time of first maximum brightness by Fitzsimmons et al. (1996). After that moment, some material starts to cross below the illumination limit, whereas no other material is capable of reaching the sunlight level (in Fig. 4a, the 6 km/s curve does not intercept the 6 km/s sunlit level). Then, the visible flux starts to decrease. For H, we see the first maximum 430 s after impact (Fig. 1) which would require slower ejecta, but the time sampling is

not good enough to conclude that. We suggest that the minimum in the lightcurves occurs when a considerable part of the material (that ejected at velocities between 7.5-9 km/s) crosses the level illuminated by sunlight on its descent, after which the amount of reflected light observed decreases. The minima in the lightcurves for H and L occur at 720 ± 100 sec and 720 ± 20 sec after impact, respectively, according to Fig. 1c. This is in agreement with predictions in Figs. 4a, 4b, for the disappearance of 9 km/s ejecta.

The following maximum in the CCD lightcurve arises mainly from thermal emission by the particulates or gas, as well as from reflected sunlight from the rest of the plume. The thermal emission starts to decrease as the material cools down and the small fraction of ejecta which was thrown highest (velocity 12 km/s) reaches the original level (where there is no longer reflected sunlight contributing to the thermal emission). Following Figs. 4a, 4b, the 12-km/s velocity material reaches the initial level 1000 seconds after the explosion.

4. Discussion and comparison with near-infrared lightcurves

We can estimate the atmospheric depth where the emission arose at the last maximum in the CCD lightcurves. For L, the flux at 892 nm was $1.05 \pm 0.15 \cdot 10^{-11} \text{ W/m}^2/\mu\text{m}$ (calibrating the lightcurve presented by Schleicher et al., 1994 in the way described in the note on absolute calibrations and adding a 10% uncertainty associated with this procedure) and $1.22 \pm 0.09 \cdot 10^{-11} \text{ W/m}^2/\mu\text{m}$ for 907 nm (Fitzsimmons et al., 1996).

We can provide an estimation of the methane abundance by the following means: Using ($\mu = 0.15 \pm 0.02$), derived from the expected position of the ballistic ejecta as a function of time, and the methane absorption coefficient for the appropriate wavelength (K_λ), with K_λ computed for the spectral resolution of each measurement by convolving methane absorption coefficients (Karkoschka, 1994) with their respective filter transmission curves, we can determine the abundance (a):

$$I(907, t_1) = I^{emitted}(907, t_1) \exp(-K_{907}a/\mu(t_1)) \quad (1)$$

$$I(892, t_1) = I^{emitted}(892, t_1) \exp(-K_{892}a/\mu(t_1)) \quad (2)$$

assuming $I^{emitted}(892, t_1) \simeq I^{emitted}(907, t_1)$. I is the observed intensity and t_1 is a given time. Solving for a we get $a = 2$ m-Am of methane, which corresponds approximately to 1 km-Am of jovian atmosphere, assuming a constant methane molar fraction of $2 \cdot 10^{-3}$. This corresponds approximately to the 25-mbar pressure level. We have computed the fractional error in a due to the propagation of errors in intensities, absorption coefficients and μ . The resulting 1-sigma fractional error is ~ 2 . This large error arises mainly from the uncertainty in the absolute fluxes. The resulting uncertainty in pressure gives 25^{+65}_{-25} mbar.

For H, the flux at the 892-nm filter shown in Fig. 1b is (4 \pm 1) times lower than that at 948 nm, which would imply thermal

emission from the 60-mbar level. On the other hand, there is a 2-min time difference between the analyzed fluxes, which is probably quite significant. The time difference would reduce by a factor of 2 or 3 the 948-nm absolute flux at the time of the 892-nm observation, if we assume a lightcurve similar to that of Schleicher et al. Assuming a decrease by a factor of 2.5, we get an abundance of 0.003 km-am of methane, corresponding to an emission level located at 35 mbar (note that the filters used in the H observations were much narrower than for L). By estimating the propagation of 1-sigma errors, we derive $P = 35^{+30}_{-35}$ mbar.

One must note that 1 to 20 mbar is the preferred range of pressures for the impact-generated hazes at the outlying regions (West et al. 1996) as determined from post-impact HST observations and is also in agreement with the reflectivities observed at the opaque 2.3- μm region. If the aerosols were generated before their descent, then they came to a complete stop not much deeper than 20 mbar. This is close to the levels that our observations suggest. If this is really the case, then the dark aerosols “survived” the heating of the fall-back without vaporizing. This may give an indication of the kind of composition of the haze aerosols, since many of the proposed solids would vaporize at the fall-back temperatures.

From the fluxes reported for L impact at 907 nm by Fitzsimmons et al., we cannot make an estimate of the temperature of the emitting region unless we assume a certain solid angle for emission or have another flux value at another wavelength in the visible. To be detectable in the visible, the second maximum would require temperatures in excess of 1800 K, assuming Stefan-Boltzman law and very good observing conditions (with observing conditions as favorable as those described here the flux at 550 nm should be larger than $10^{-12} \text{ W/m}^2/\mu\text{m}$). In the near future we plan to conduct a search for detection of this second maximum in several data sets as well as to model the outgoing radiation from an emitting-absorbing-scattering medium.

The order of magnitude difference in flux emission for L and H may be related to very different temperatures of the plumes or to the different area of emission, or both. Our preferred explanation is that the difference is a result of the different amount of material ejected in the 9-12 km/s velocity range.

The steep rise in the 2.3-micron near-infrared curves for impacts H and L, 49 ± 12 sec and 39 ± 3 sec after impact respectively (the beginning of the second precursors) can be explained by emission from the highest velocity ejecta reaching the level of the limb as seen from the Earth. These ejecta must have $v = 9 \pm 1$ km/s (see Fig. 5). Velocities higher than this would have resulted in earlier detections. The impact times were adopted from the Galileo PPR lightcurve (Martin et al., 1995) and the near-infrared lightcurves and timings are those by Hamilton et al. (1995). From this determination, the fastest material which is optically thick enough to radiate measurable quantities is moving at 9 ± 1 km/s, the same as the determination made using the first detection of the plume in visible light (9 ± 1 km/s).

The maximum in the second precursor may occur when no additional material can reach the limb level (ejecta slower than 3.5 km/s). In Fig. 5 we see that no further material can reach this level after 200 s. Then, the maximum should be around this

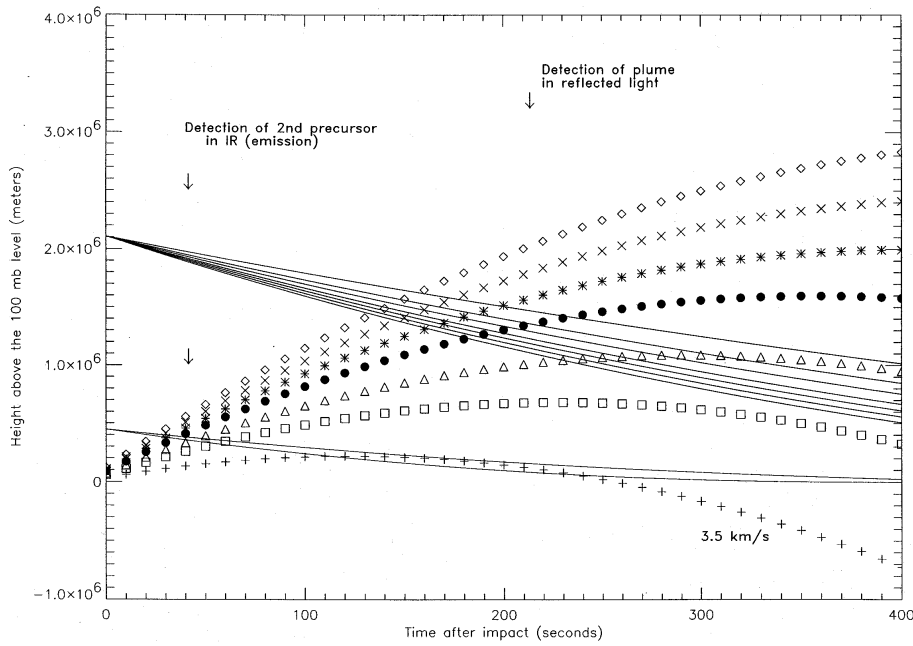


Fig. 5. Enlargement of Fig. 4a for short times after impact. Also in this graph has been included the height as a function of time for 3.5-km/s ejecta, which are the slowest ejecta which can reach the limb height and be detectable in emission

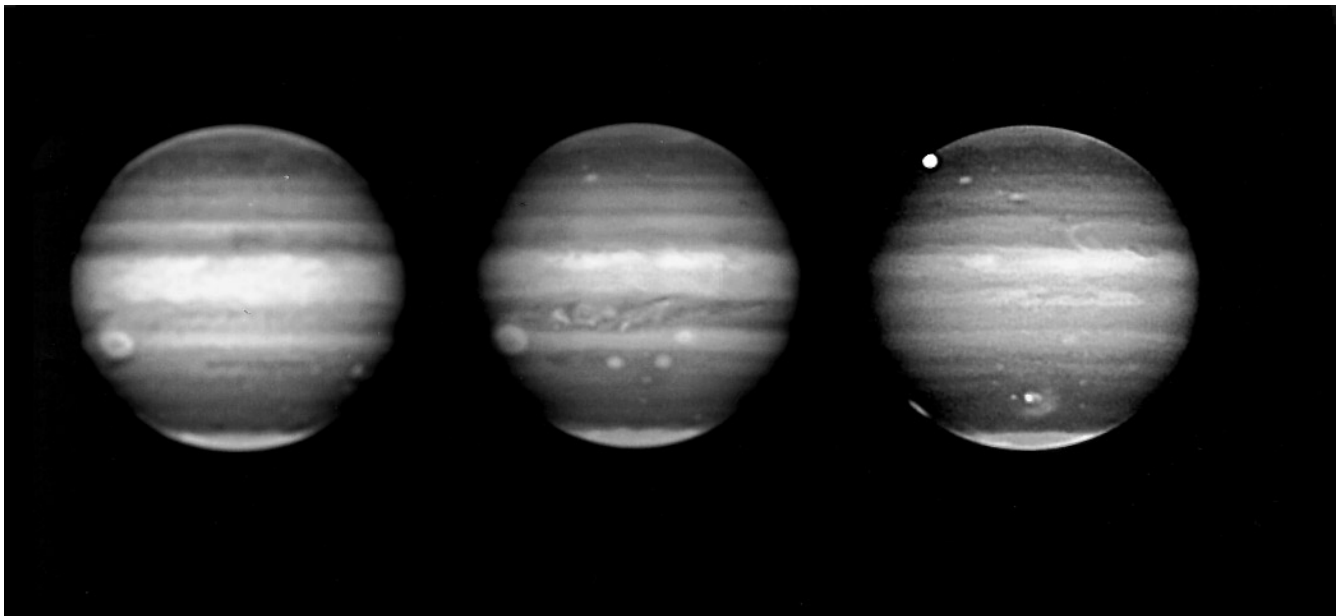


Fig. 6. Images at 892 nm from three consecutive years (from left to right: 1992,1993,1994). The image from 1994 shows the D and G impact areas close to the Central Meridian. The bright area at the terminator is the H impact scar and the bright spot at the upper left is satellite Ganymede. There is a clear temporal variation in reflectivity at equatorial latitudes

time, for the second precursors. However, the plume is cooling while going up, and that may change the predicted behavior by a large amount. We see the second precursor peak about 180 s after H impact which is considerably close to the estimate. The maximum of the L second precursor seems to occur before the predicted time. The beginning of the main near-infrared peak would correspond to the fall to the original levels of ejecta with 4 km/s initial velocity.

As we have already pointed out, the 2.3- μm maximum occurs earlier than the CCD second maximum. The 2.3- μm peak may be due to the reimpacting material that was ejected at velocities lower than 9 km/s, which may represent a small fraction of the total plume or may not have enough energy to trigger the visible emission. But the total energy released in the near infrared wavelengths is higher than that at visible wavelengths, which seems to be contradictory with the idea that the ejecta

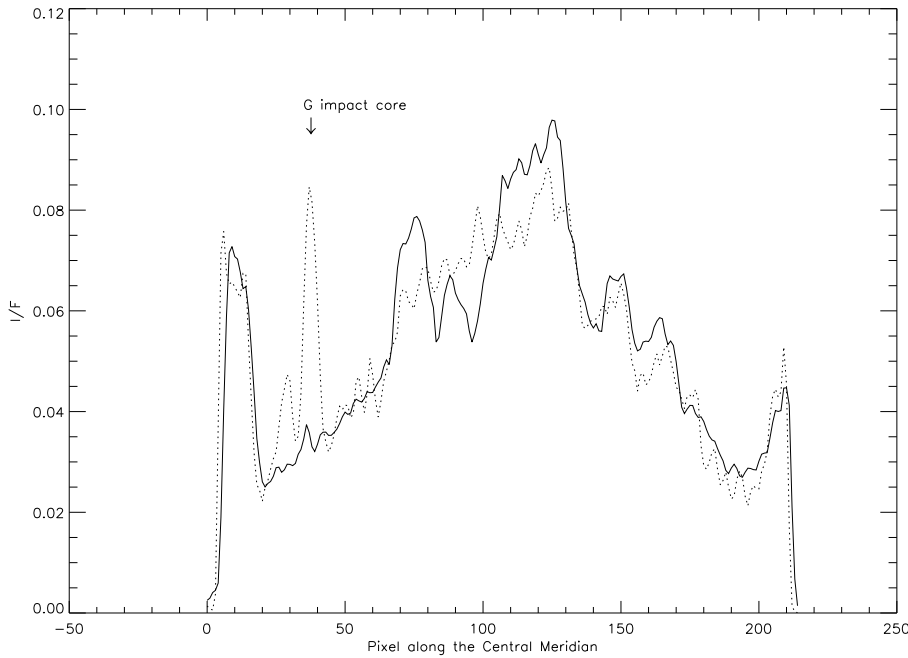


Fig. 7. Comparison of Central Meridian scans from 1993 and 1994

with velocities lower than 9 km/s constitute a small fraction of the plume.

One solution is to hypothesize that the particulates are optically thick in the visible, but the gas is optically thin. As the particulates are optically thick to reflected sunlight, they should also be efficient thermal emitters. If the particulates were the only material which emitted in the visible, the emission could be delayed in this wavelength range compared to the near infrared because the particulates were concentrated in the ejecta with $v=11$ km/s. It is still a matter of speculation why the particulate ejecta were concentrated in a certain range of velocities, but that supposition is also supported by the arc shapes of the scars, as opposed to a continuous semidisk shape.

An alternative explanation for the difference in the timings of the visible vs near-infrared emission maxima is that the infrared emission took place hundreds of kilometers above the visible emission level. There, the friction might have been enough to radiate in the near infrared, but not in the visible, as the material was not hot enough or was not sufficiently optically thick in the visible.

5. Summary

Assuming a fairly narrow distribution of velocities for 45° ballistic trajectories, we can explain several of the features observed in our H lightcurve as well as in published lightcurves for the L impact. We can also explain some of the features in the near-infrared lightcurves. In particular, the time of the first detection of the plume at visible wavelengths is accounted for by 9 ± 1 km/s ejecta, which comprise most of the plume and the 11-km/s ejecta are responsible for the second maximum in the CCD lightcurves. The 9-km/s ejecta are also responsible for the beginning of the second precursor seen at near-infrared

wavelengths and for the main peak. The first maximum in CCD lightcurves is at its widest phase in height and the maximum amount of material is exposed to sunlight. A fraction of the plume, the portion with velocities lower than 9 km/s, is responsible for the minimum when it disappears from direct solar illumination in the descending part of the trajectory. The CCD emission in the second maximum originates at pressures 25^{+65}_{-25} mbar and 35^{+30}_{-35} mbar for the L and H impacts, respectively. The near-infrared peak occurs before the second maximum in the CCD lightcurves.

We note that further elucidation of these processes will be possible when additional synoptic observations of the H and L impacts at shorter wavelengths are considered. This will give us a better description of the thermal behavior of the ejecta from its continuum emission. Ultimately, the most quantitative progress will be made by extending these calculations to a spatially inhomogeneous thermophysical model for the ejecta which is coupled with appropriate radiative transfer calculations. These can then be compared with Galileo and earth-based observations at a variety of wavelengths.

6. Notes on absolute calibrations

Outside the deep methane bands the absolute fluxes have been calibrated using 1993 albedos by Karkoschka (1994) and solar fluxes from Neckel and Labs (1984). However, for the jovian planets, the use of disk albedos from different dates at methane bands may not be appropriate. In the case of Saturn, remarkable reflectivity changes at equatorial latitudes have been reported recently (Ortiz et al., 1995), and we have also found changes at the equatorial latitudes in Jupiter, from 1993 to 1994 (see Fig. 6). The equatorial band is broader and more reflective during 1992 and 1993 than the 1994 observation. Comparing our absolutely

calibrated images from 1992 (Moreno et al., 1993) with non flux-calibrated images from 1993, and 1994, we conclude that there is a *decrease* in the albedo of Jupiter at 892 nm. We have estimated this change using central meridian scans from 1993 and 1994, scaled to the latitudes where the reflectivity is nearly constant during the 3 different years. We chose that region by normalizing each image (that is, dividing the data numbers at each pixel by the total counts from Jupiter) taking a Central Meridian scan from each one and comparing the plots. This, to first order, helps us identify the regions with lowest variability. By integrating the reflectivities in Fig. 7 (removing the contribution from the G impact scar), our conclusion is a 5% *decrease* from 1993 to 1994. This is in agreement with Moreno et al. 1995 who found a small decrease, or no change from 1993 to 1994, using the jovian satellites as a reference, but not the 10% *increase* suggested by West et al. (1995). We have used a lower albedo (5%) than that of Karkoschka (1994), for the 892-nm filters in 1994.

Acknowledgements. We are grateful to Jose Ruedas at the Instituto de Astrofísica de Andalucía for helping us read two corrupted data files. We are also grateful to H. Schleicher and A. Fitzsimmons for providing us with the lightcurves shown in Fig. 1c. A. Fitzsimmons' careful review of the paper is greatly appreciated. The 4.2-m William Herschel Telescope is operated on the island of La Palma by the Royal Greenwich Observatory in the Spanish Observatorio del Roque de los Muchachos of the Instituto de Astrofísica de Canarias. This research was performed at NASA/Jet Propulsion Laboratory, California Institute of Technology. JLO, FM and AM were supported by the Comisión Nacional de Ciencia y Tecnología under contracts ESP94-0719, ESP94-083, and ESP93-0338. GO and PYF were supported by the NASA Planetary Atmospheres Program.

References

- Anderson, J. D., 1976, in: Jupiter, eds. T. Gehrels, The University of Arizona Press, Tucson, Arizona, p. 113
- Fitzsimmons, A., et al., 1995, *MNRAS*, 278, 781
- Graham, J. R., et al., 1995, *Science*, 267, 1320
- Hammel, H., et al., 1995, *Science*, 267, 1288
- Hamilton, D. P., et al., 1995, *Geophys. Res. Lett.*, Vol 22, 17, 2417
- Herbst, T. M., et al., 1995, *Geophys. Res. Lett.*, Vol 22, 17, 2413
- Karkoschka, E., 1994, *Icarus*, 111, 174
- Lagage, P. O., et al., 1995, European SL-9/Jupiter workshop, ESO Conference and Workshop Proceedings No 52, p. 147
- Larson, S., et al., 1994, *Suppl. to Bull. Amer. Astron. Soc.*, 26, p. 7
- Lucy, L. B., 1974, *ApJ*, 79, 745
- Martin, T. Z., et al., 1995, *Science* 268, 1875
- Moreno, F., et al., 1995, *Geophys. Res. Lett.* Vol. 22, 12, 1609
- Moreno, F., Molina, A., Ortiz, J. L., 1993, *J. Geophys. Res.*, 98, 18837
- Neckel, H., Labs, D., 1984, *Sol. Phys.*, 90, 205
- Nicholson, P. D., 1996, in: *The Collision of Comet Shoemaker-Levy 9 and Jupiter*, eds. K. S. Noll, H. A. Weaver, P. D. Feldman, Cambridge University Press, Cambridge, p. 81
- Nicholson, P. D., et al., 1995, *Geophys. Res. Lett.*, Vol. 22, 12, 1613
- Ortiz, J. L., 1994, *Vertical cloud structure in Jupiter and Saturn based on CCD spectrophotometry between 0.6 and 0.95 μm* , Thesis, Univ. Granada
- Ortiz, J. L., Moreno, F., Molina, A., 1995, *Icarus*, 117, 328
- Orton G., et al., 1995, *Science*, 267, 1277
- Schleicher, H., et al., 1994, *Earth, Moon and Planets*, 66, 13
- Takeuchi, S., et al., 1995 *Geophys. Res. Lett.* Vol. 22, 12, 1581
- West R. A., 1996, in: *The Collision of Comet Shoemaker-Levy 9 and Jupiter*, eds. K. S. Noll, H. A. Weaver, P. D. Feldman, Cambridge University Press, Cambridge, p. 269
- West, R. A., et al., 1995, *Science*, 267, 1296